Improved Impingement Cooling Using Flow Enhancing Structural Elements

M. Schroll[1,*], C. Willert[1], C. Morsbach[2], M. Matha[2], R. Brakmann[3]

1: Measurement Technology, Institute of Propulsion Technology, German Aerospace Center (DLR), Cologne, Germany
2: Numerical Methods, Institute of Propulsion Technology, (DLR), Cologne, Germany
3: Turbine, Institute of Propulsion Technology, (DLR), Göttingen, Germany

*Corresponding author: michael.schroll@dlr.de

Keywords: turbine blade cooling, jet impingement, heat transfer, jets, cross-flow, turbulence, Reynolds-averaged Navier-Stokes simulation, RANS, high-speed PIV, modal decomposition, POD, spectral proper orthogonal decomposition, SPOD.

ABSTRACT

This investigation is part of a study seeking to improve impingement cooling in internal combustion turbomachinery using flow modifying elements within the cooling channel. A simplified geometry of a jet impingement cooling configuration is chosen for well-defined numerical simulations and complementary experiments. The generic cooling channel setup features of a square cross-section that is closed on one end and is supplied by 9 inline jets that are directed toward a heated plate. Using RANS, the presence of an arc-conic placed immediately downstream of each jet nozzle was found to increase the heat transfer and prompted the present experimental study to elucidate the fluid mechanical mechanisms leading to the improved performance. Central to the study is an extensive data base of time-resolved 2d-2c PIV data for both channel configurations, with and without installed arc-conics, on a field of view that simultaneously captures up to 3 jets. Using two-point correlations, an interaction or modal coupling between the jets is not observed, suggesting that each jet may be treated individually. The arc-conics tend to stabilize the jets by capturing and redirecting the bulk cross-flow, thereby increasing the self-similarity of the jet impingement pattern, in particular toward the channel exit. Modal analysis using both proper orthogonal decomposition (POD) and spectral proper orthogonal decomposition (SPOD) capture the dynamics of the flow, ideally to achieve a dimensionality reduction for reduced order modeling. However, the fully turbulent flow with highly stochastic dynamics exhibits only weak spatial or temporal signatures, with the energy content spread across a large number of modes. Among the dominant modes are pulsations of the jet onto the surface along with spanwise sweeping motions. The stabilization of the jet by the arc-conic results in a more defined impingement flow with the signature of the jet's shear layer visible in the higher modes of the energy spectrum and is considered the main mechanism of improved heat transfer.

---

available at https://elib.dlr.de/204728/

1. Introduction

The further improvement of combustion driven turbomachinery requires an increase of the combustor exit temperature. At same time the integrity of the downstream high pressure turbine stages must be maintained with adequate cooling of the turbine blades. As the increased use of cooling air sourced from the high-pressure compressor directly affects the thermodynamic performance of the engine, efficient cooling strategies are crucial. Well established is the use of impingement cooling on the inside of turbine blades using arrays of small air jets. The underlying design rules are generally based on conservative correlations and proven configurations. Any further improvement of the engine's performance requires the re-assessment of established cooling concepts toward more unique strategies. The present work is part of a multi-disciplinary effort aimed at further improving the understanding of the underlying heat transfer mechanisms of jet impingement cooling using both experiments and numerical simulation of a well conditioned reference configuration (Schroll et al., 2022; Tabassum et al., 2023; Morsbach et al., 2024). The focus here is on improving the heat transfer on the impingement wall by altering the flow geometry of impinging air jets through passive means such as topology modification or by harnessing self-excited flow modulation. In the scope of this work, the potentials of low order modelling of the impingement cooling flow are investigated by applying modal decomposition on the flow field data.

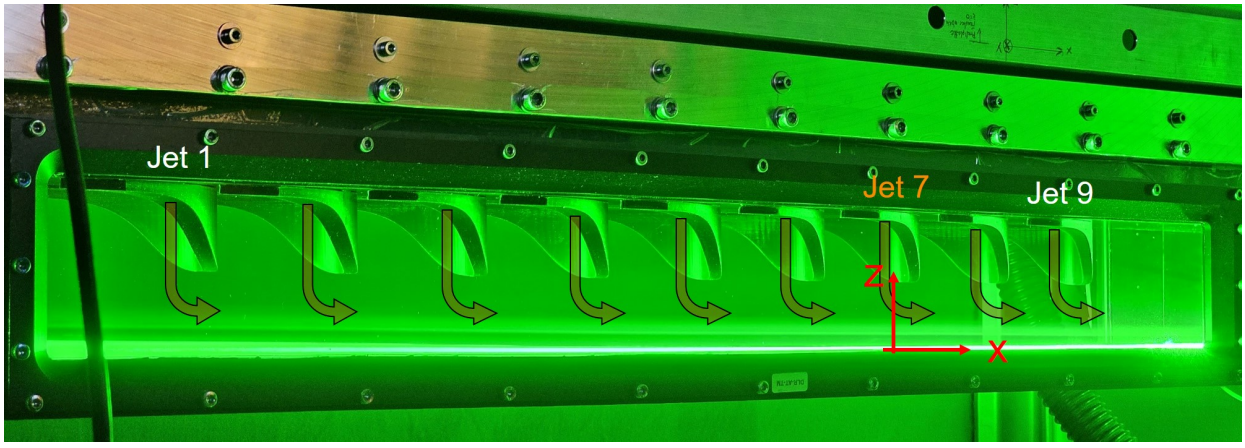

Figure 1. Impingement cooling configuration with installed arc-conics. Laser light sheet for HS-PIV is parallel to bottom surface (target plate) spanning the xy-plane.

2. Flow facility

The study is performed on a generic multi-jet configuration that lends itself to be both well modeled numerically as well as experimentally. Fig. 1 shows a photograph of the actual experiment. A total of 9 jets with a diameter of $D = 15.2\,\mathrm{mm}$ issue into a square test section of size $5D \times 5D$, with the jets spaced linearly at intervals of $5D$. With one end of the square channel sealed, a mean flow

establishes itself with the velocity increasing toward the exit and the deflection of the individual jets gradually increasing. The seventh jet is of particular interest as it is fairly similar to its neighbors and still impinging on the surface, while the last jet No. 9 begins to lift off. The geometry has been studied numerically using Reynolds-averaged Navier–Stokes simulation (RANS) by Tabassum et al. (2023) and large-eddy simulation (LES) by Morsbach et al. (2024). A sample snapshot from the LES is provided in Fig. 2 and gives an impression of the highly dynamic nature of the turbulent flow within the square cooling channel. With the Nusselt number as a measure of the heat transfer efficiency, the mean flow results in a characteristic temperature distribution on the cooling plate, such as shown in Fig. 3. The presented data was obtained through RANS and indicates a decreasing cooling efficiency from left to right (toward the channel outlet). While the first row in Fig. 3 was obtained for a smooth wall, the temperature distribution (and cooling efficiency) is altered through surface modifications such as V-ribs (middle row) or arc-conics (bottom row). The use of rib-structures placed on the surface to be cooled has been extensively investigated in the past, the current study focuses on modifications of the jets themselves, such as by placing arc-conics near the jet orifices. As empirically investigated by Brakmann et al. (2023) using RANS, the arc-conics were found to stabilize the jets resulting in a more efficient cooling towards the channel exit (Fig. 3, bottom row).

Within the present work, the optimal arc-conic configuration determined by RANS is experimentally investigated, mainly through the use of planar, high-speed particle image velocimetry (PIV) and compared to the reference case without arc-conics (smooth wall). By substantially increasing the field of view in comparison to previously reported measurements (Schroll et al., 2022), possible inter-jet dynamics can be captured. Ultimately, correlations between near wall velocity field and temperature distribution, available through measurement or from numerical simulation, are used to approximate the temperature distributions of the modified geometries.

3. High-speed PIV measurements and processing

Most of the high-speed PIV (HS-PIV) measurements reported herein are performed with a pair of beam-coupled, diode-pumped pulsed Nd:YVO_4 lasers each with a rated pulse energy of 1 mJ at 40 kHz (Iradion/Innolas Blizz 532, pulse width $\leq 12\,\mathrm{ns}$). A constant width light sheet exceeding 50 mm is achieved using a large diameter plano-convex lens with a focal length of $f = 450\,\mathrm{mm}$ as part of the light sheet forming optics. A low beam divergence of 2.5 mrad coupled with a spatial mode of $M^2 \leq 1.4$ allows the laser beam to be collimated across a relatively wide domain such that several jets can be captured simultaneously.

The light-sheet illuminated aerosol droplets (atomized $1\,\mu\mathrm{m}$ paraffin oil) carried by flow are recorded using a high-speed camera with a detector size of 2560×1664 pixel a pitch of $9.27\,\mu\mathrm{m/pixel}$ (Vision Research T4040). To achieve framing rates up to and beyond 20 kHz while covering up to 3

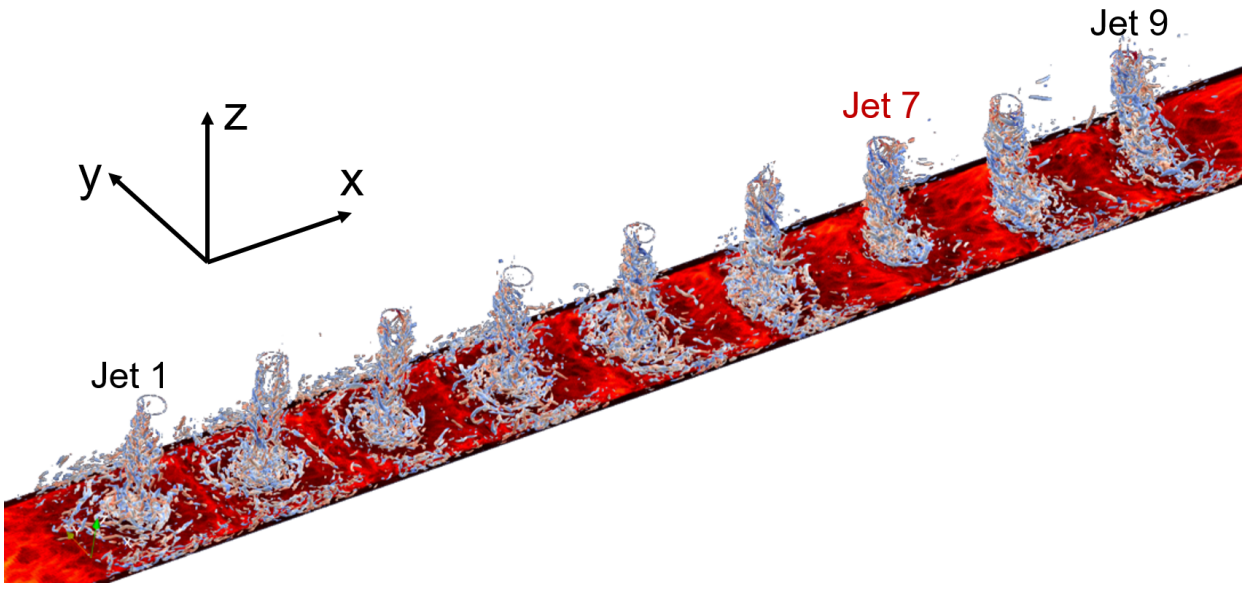

Figure 2. Snap-shot from LES of "clean" configuration showing vorticies as contours of the Q-criterion coloured with streamwise vorticity and wall temperature distribution (Morsbach et al., 2024).

jet domain ($15D$, 230 mm), the active domain of the sensor is reduced to 576 or 608 lines (see Table 1). Using a 105 mm lens (Nikon Micro-Nikkor 105/2.8) at an aperture of f/4 the field of view (FOV) is imaged with magnifications of $94.1\,\mu\mathrm{m/pixel}$ or $43.4\,\mu\mathrm{m/pixel}$.

3.1. Measurement configurations

For HS-PIV the measurement domain covers up to 3 jet intervals axially ($15D$) and about $60\,\%$ of the channel width. This is substantially larger than for the previously reported measurements by Schroll et al. (2022) and is made possible with the improved hardware described earlier. The

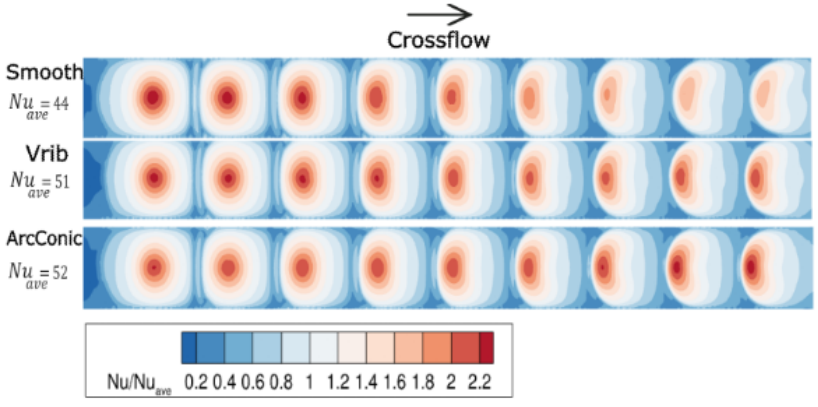

Figure 3. RANS prediction from Brakmann et al. (2023) of the Nusselt number distribution for clean (top), V-rib structured wall (middle) and arc-conic configuration (bottom).

Table 1. Overview of acquired PIV data

Domain		**Jets 6–9**	**Jets 6–9**	**Jet 8 only**
Plane		xz ($y = 0$)	xy ($z \gtrsim 0$)	xy ($z \gtrsim 0$)
FOV	[pixel]	2560×480	2560×576	608×1536
	[mm^2]			
Magnification, M	[$\mu\mathrm{m}$/pixel]	94.1	94.9	43.4
Number of frames, N_f	-	71 209	59 361	94 242
Number of records, N_{rec}	-	4	4	2
Record duration, t_{rec}	[s]	2.97	3.56	3.77
Flow-through times	[L (=5D)]	75-100	90-120	111
Grid size, $N_x \times N_y \times N_z$	-	$319 \times 1 \times 59$	$318 \times 70 \times 1$	$75 \times 191 \times 1$
Sample volume, $\Delta_x \times \Delta_y \times \Delta_z$	[mm^3]	$1.5 \times 1.0 \times 1.5$	$2.3 \times 2.3 \times 1.0$	$0.69 \times 0.69 \times 0.5$

enlarged FOV also addresses the conjecture of possible inter-jet interactions. Table 1 gives an overview of the data base of various measurements configurations. Along the symmetry plane at $y = 0$ the jet impingement across 3 adjacent jets is simultaneously captured and intends to document the change in deflection of the jet due to geometry modifications, Corresponding measurements in the xy-plane parallel to target plate $z \gtrsim 0$ are intended to capture the near-wall dynamics, in particular, to provide qualitative maps of wall-shear stress distribution (c.f. Depardon et al., 2005). Using a higher magnification, details of the impingement region with a thinner light sheet closer to surface are acquired near jet No. 8.

All measurements are acquired at a constant mass flow rate of $\dot{m} = 20\,\mathrm{g/s}$ such that the bulk Reynolds number of the jets corresponds to $\mathrm{Re}_D = 10\,000$ with a mean jet bulk velocity of $U_0 \approx 10.2\,\mathrm{m/s}$. For each light sheet configuration and flow geometry up to 4 records are acquired at frame rates of $20\,\mathrm{kHz}$ or $25\,\mathrm{kHz}$. The average duct flow velocity increases with increasing mass flow over the duct length due to the successive incoming jets. In the square cross-section of size $5D \times 5D$, this velocity increases from $1.9\,\mathrm{m/s}$ behind jet No. 6 to up to $2.9\,\mathrm{m/s}$ behind jet No. 9. Within in a measurement time of $3\,\mathrm{s}$ a flow domain up to $8.6\,\mathrm{m}$ is moving, giving a flow-through-time of $113\,\mathrm{L}$ behind jet No. 9 and in comparison $75\,\mathrm{L}$ behind jet No. 6.

3.2. PIV processing

The acquired high-speed image records are analyzed with a cross-correlation based triple-frame scheme that improves the data yield while reducing the noise level. Prior to $N = 100$ block-wise batch processing, the mean intensity is subtracted followed by histogram clipping at 98^{th} percentile (Shavit et al., 2007) and low-pass filtering, the latter in order to reduce pixel-locking bias. A grid-refining approach begins with samples of 96×96 pixel and iteratively refines to either 24×24 (xz-plane) or 16×16 pixel for the near-wall xy-plane. A 50% overlap is applied. Validation using a normalized median filter (Westerweel & Scarano, 2005) with a cutoff at 3.0 yields validation rates exceeding 99%. Processing on a 32-core PC system (Intel Xeon W2295 3 GHz) requires about $6\,\mathrm{h}$

per record of 108 GB size. The resulting two-component velocity data is compiled into multiple blocks of $N_f = 20\,000$ for the subsequent post-processing steps presented next.

4. Results

Two different flow conditions are investigated and compared in this study:

Reference case without any modification of the channel surfaces and has already been subject of a previous studies using PIV and unsteady TSP (Schroll et al., 2022), RANS (Tabassum et al., 2023) and LES (Morsbach et al., 2024),

Arc-conic case has arc shaped structures installed on the jet plate as shown in Fig. 1 and has been subject of a RANS study by Brakmann et al. (2023).

All measurements are performed at the same mass flow rate, that is, fixed jet nozzle velocity, to ensure an optimal basis for comparison.

4.1. Visualization of the velocity records

Fig. 4 presents exemplary space-time records (kymograms) for both flow configurations. The records are compiled by extracting the time-varying profile of near-wall velocity data along a fixed line spanning the channel. The data is collected from spanwise lines positioned at $x/D = 5.8$ and $x/D = 5.2$ for the reference and arc-conic configuration, respectively. These positions are chosen near their slightly offset mean stagnation point of the impinging jet, specifically jet No. 8. The plots showcase several aspects:

- The reference case is dominated by large scale jet bursts, related to the intermittent, partial lift-off of the jet.
- The arc-conic configuration shows a high-frequency modulation of the jet with rare interruptions. These begin near the symmetry line ($y = 0$) and propagate outward.
- None of the velocity records indicate a pronounced periodicity and show a spanwise meandering of the stagnation point.

The streamlines presented in Fig. 5 provide a clear indication that the arc-conics straighten the flow allowing the jets to impact on the surface in a near normal direction. Overall, the flow patterns have an increased level of self-similarity across the jets, contrary to the increased level of deflection in the reference case, where jet No. 9 (at position $x/D = 10$) begins to detach from the wall.

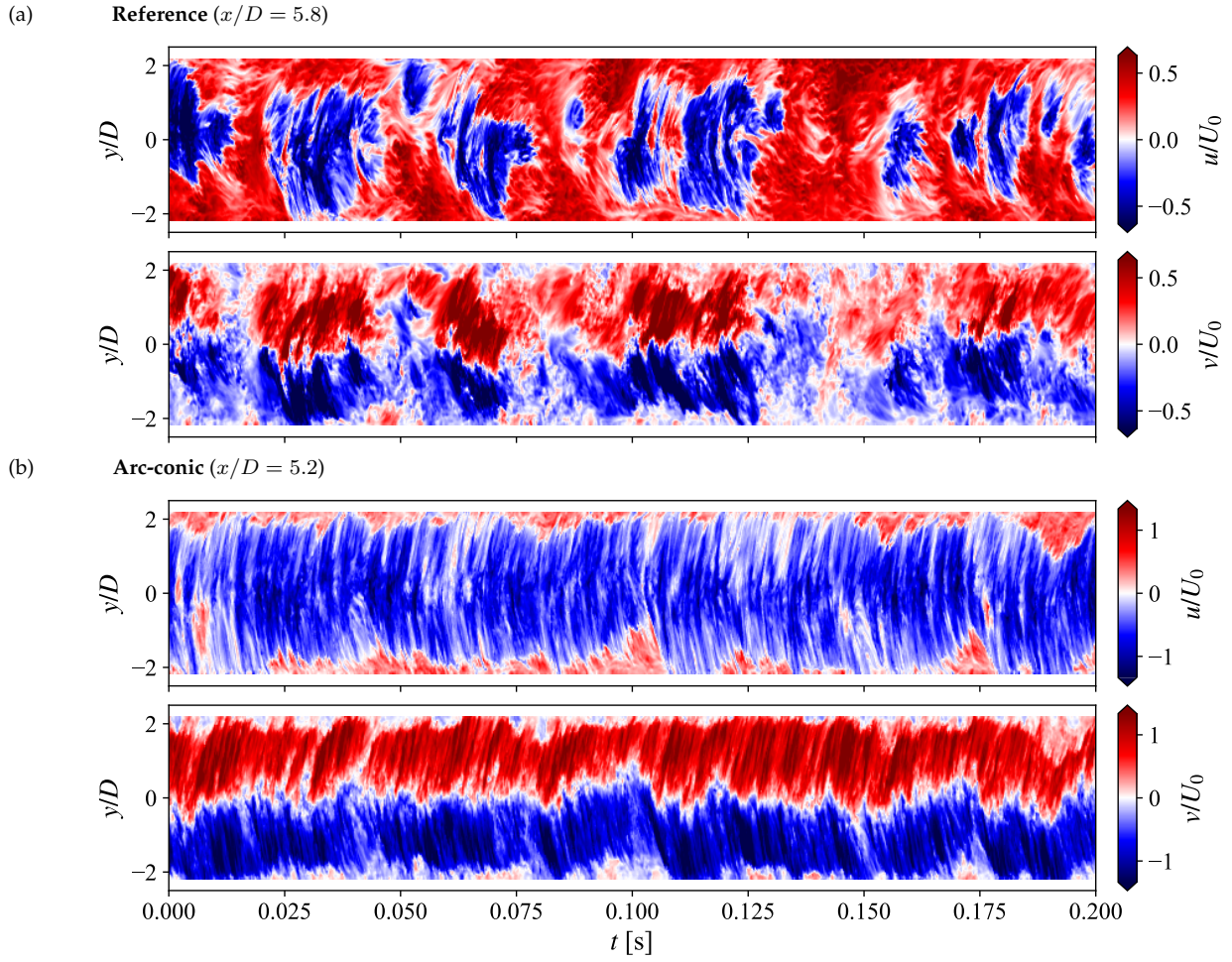

Figure 4. Space-time visualization (kymogram) of the velocity components along a fixed line spanning the wall-parallel plane for the reference configuration (a) and with arc-conics (b).

Fig. 6 provides a topological impression of the near-wall flow field for the two configurations. Source and saddle points are determined using the critical point analysis procedure proposed by Perry & Chong (1987). While the streamline patterns are very similar between the configurations, the positions of source points (i.e. jet stagnation points) and saddle points are shifted. For the arc-conics configurations they are at nearly similar positions with respect to the jet orifices. The near-wall flow fields are also qualitative representations of the wall shear stress field as demonstrated by Depardon et al. (2005). Earlier measurements on the same flow provide estimates of viscous length scales ν/U_τ in range of $27\,\mu\mathrm{m}$ to $40\,\mu\mathrm{m}$ (c.f. Schroll et al., 2022). The light sheet intensity peak is located about $0.5\,\mathrm{mm}$ from the wall which corresponds to roughly 15 viscous units, so clearly located in the buffer region of the (unsteady) turbulent boundary layer. Nonetheless, velocity scales and measurement configurations are similar to those reported by Depardon et al. (2005) who observed a strong agreement between oil-flow visualization and near-wall PIV measurements.

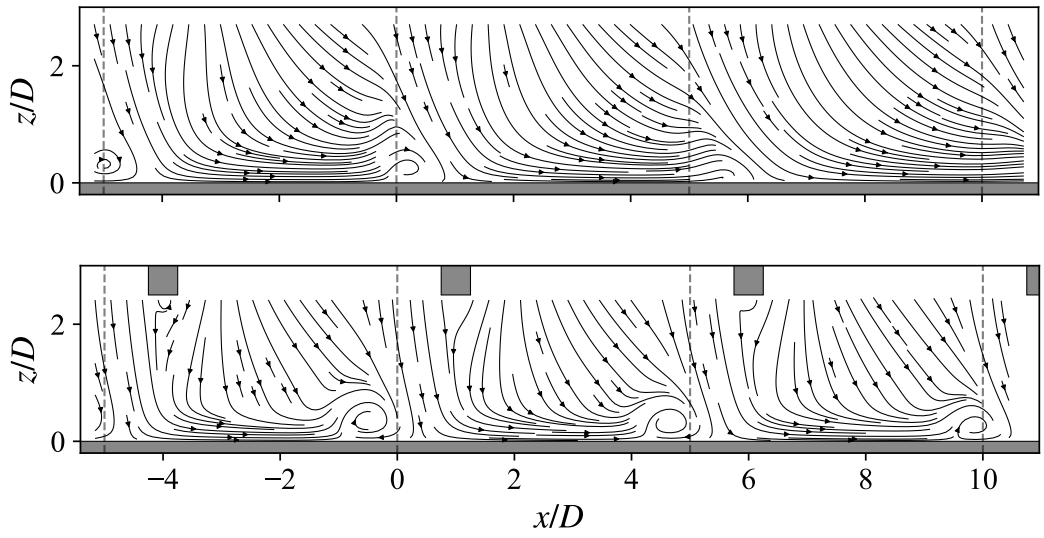

Figure 5. Mean streamlines at the symmetry plane ($y = 0$) for reference case (a), with installed arc-conics (b).

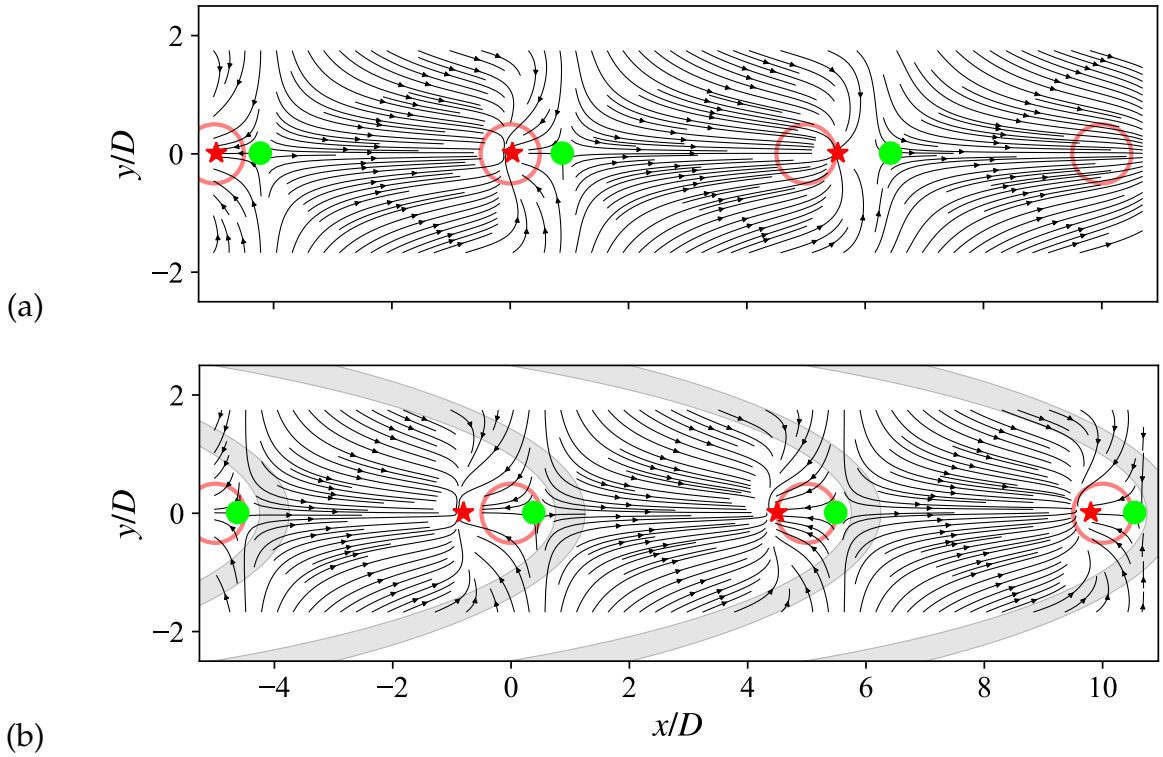

Figure 6. Mean near-wall streamlines for reference case (a) and with installed arc-conics (b). The jet nozzles on the opposite wall are indicated by red circles; symbols mark critical points: sources ●, saddle points ★.

4.2. Mean and statistics

Figures 7 and 8 present time-averaged data for the reference and arc-conic configuration, obtained with HS-PIV, respectively acquired in the wall-parallel plane close to the surface $z \gtrsim 0$ and within channel's symmetry plane at $y = 0$. All data is normalized with the jet's bulk exit velocity $U_0 \approx 10.2\,\mathrm{m/s}$.

In comparison to the reference case, the arc-conic configuration reveals significantly higher mean values, in particular in the wall-parallel xy-plane. This is attributed to the stabilization of the individual jets through the confinement provided by the arc-conic which also cause the bulk of the convective flow to move toward the cooling wall. This is particular visible for the axial velocity component U in Fig. 8. Also, the vertical movement of fluid away from the wall is restricted by the arc-conics as exhibited in the W component of Fig. 8.

4.3. Two-point correlations

Two-point correlations provide a measure of similarity between the data u_1 at a given point $\mathbf{x}_0$ in space $\mathbf{x}$ (or time) with respect to the data u_2 in its neighborhood. Here it is calculated from the velocity records $u_i = u_i\,(x, y, z, t)$ using the discrete version of the cross-correlation coefficient:

$$R_{u_i u_j}(\mathbf{x}, \mathbf{x}_0) = \frac{\int u_i'(\mathbf{x}, t)\, u_j'(\mathbf{x}_0, t)\, dt}{\sqrt{\int u_i'(\mathbf{x}, t)\, u_i'(\mathbf{x}, t)\, dt} \cdot \sqrt{\int u_j'(\mathbf{x}_0, t)\, u_j'(\mathbf{x}_0, t)\, dt}} \tag{1}$$

$$= \frac{\langle u_i'(\mathbf{x}, t) \cdot u_j'(\mathbf{x}_0, t) \rangle}{\sigma_{u_i}(\mathbf{x}) \cdot \sigma_{u_j}(\mathbf{x}_0)} \tag{2}$$

where $\sigma_{u_j}(\mathbf{x}_i)$ is the square root of the variance of all samples u_j at the point $\mathbf{x}_i$.

For both channel configurations two-point correlations are calculated using the stagnation point of jet No. 7 as a reference. For the arc-conic configuration this reference point is shifted upstream by about $0.5\,D$. Noteworthy is the strong similarity of the correlation maps shown in Fig. 9 in spite of the significant differences in the flow topology (cf. Fig. 6) and statistics (cf. Fig. 7). More importantly, neither configuration exhibits a discernible correlation of one jet with the other which is a clear indication that the jets do not interact. While not presented here, a similar conclusion was reached by extending the two-point correlation to include the time variable to reveal the temporal lag across the FOV.

4.4. Modal Analysis using POD

POD is applied to the fluctuating velocity components measured by HS-PIV in the hope of revealing the dominating spatially coherent structures. For each flow condition, the vector field records

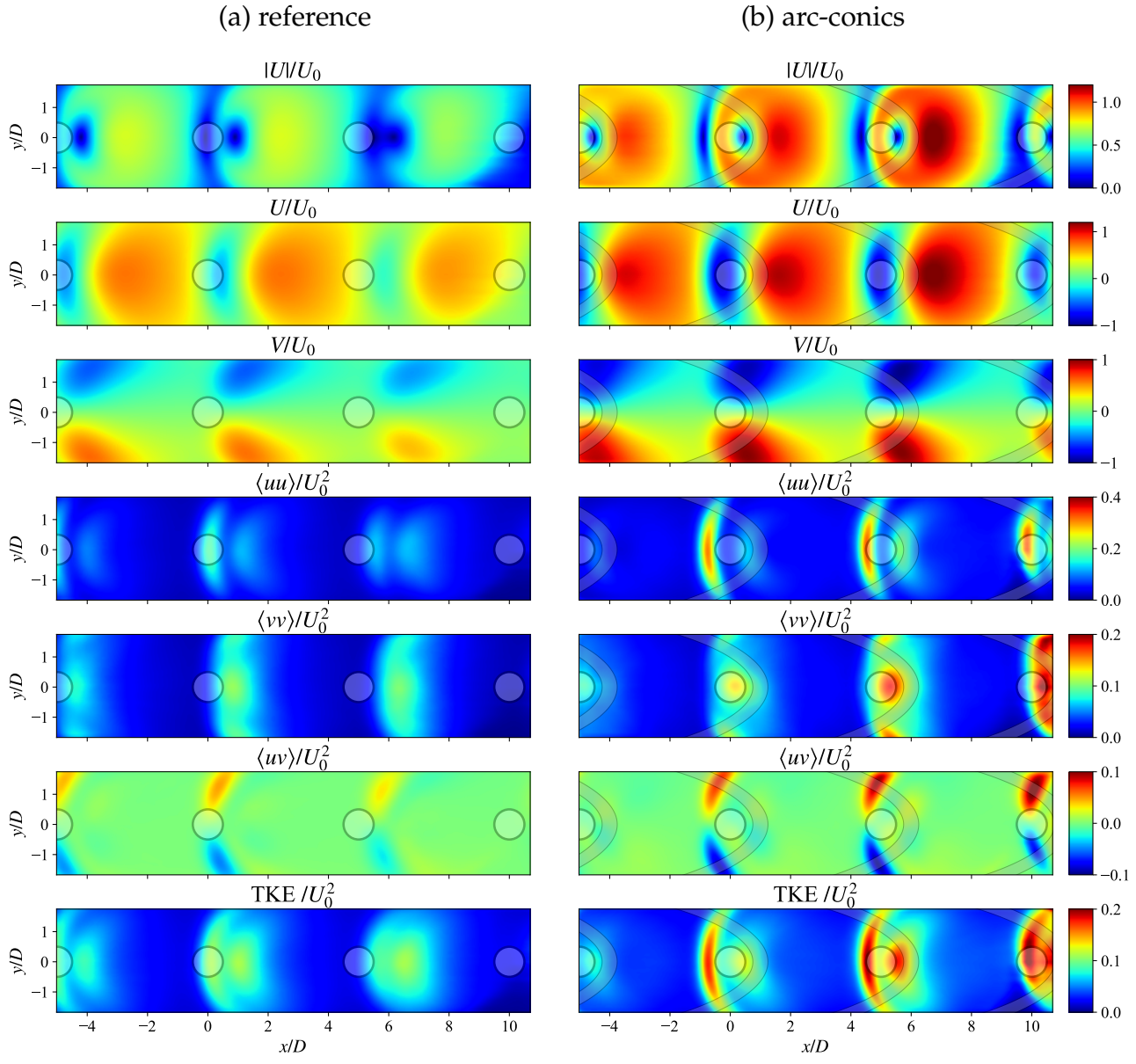

Figure 7. Mean and higher order statistics of the wall-parallel plane ($z \approx 0$) for the reference configuration (a) and with arc-conics (b). All quantities scaled with reference velocity $U_0 \approx 10.2\,\mathrm{m/s}$.

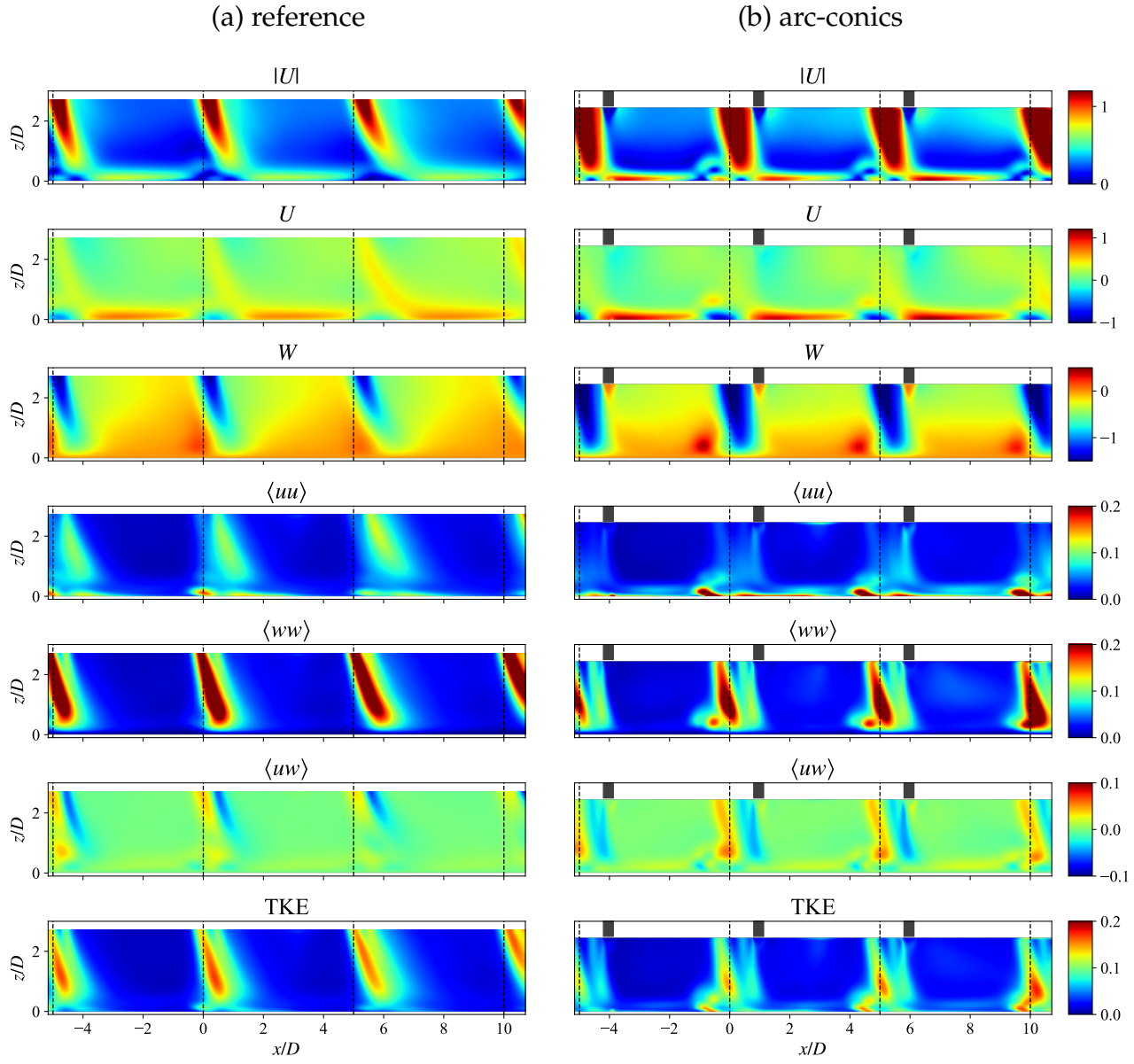

Figure 8. Mean and higher order statistics at mid-span ($y = 0$) for the reference configuration (a) and with arc-conics (b). All quantities scaled with reference velocity U_0.

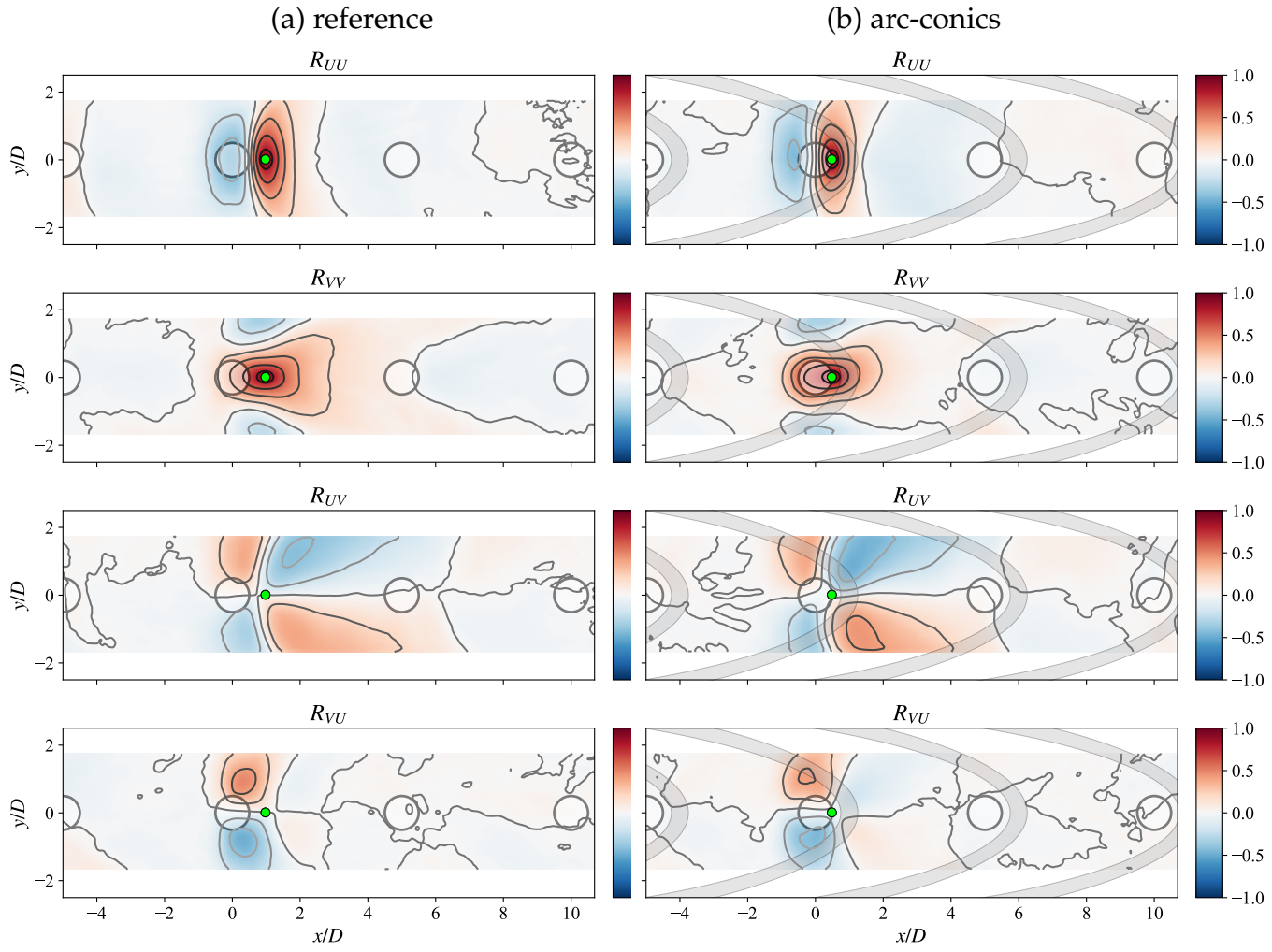

Figure 9. Two-point correlation maps in the xy-plane at $z \approx 0$ covering jets No. 6 to No. 9. Reference point is chosen near stagnation point of jet No. 7 for reference condition (a) and with installed arc-conics (b).

are decomposed into sets of orthogonal spatial modes $\phi_j(\mathbf{x}_n)$ weighted by the time coefficients a_{ij} so that:

$$\mathbf{u'_i}(\mathbf{x}_n) = \sum_{j=1}^{N} a_{ij}\, \phi_j(\mathbf{x}_n) \tag{3}$$

The matrix $\mathbf{u}'(\mathbf{x_i}_n)$ consists of up to $N_{\text{rec}} = 4$ records of N_f fields each containing of $N_{\text{tot}} = N_x \times N_y \times N_z$ vectors of two-component velocity data. Due to the large size of the problem ($N_{\text{rec}} \times N_f \times N_{\text{tot}}$), the data was down-sampled by a factor of 10, resulting in an effective sampling frequency of $2\,\text{kHz}$ or $2.5\,\text{kHz}$. Processing is implemented using the principal component analysis (PCA) routines of the *SciKit-Learn* Python package (Pedregosa et al., 2011) which make use of the *LAPACK* solver for the singular value decomposition (SVD). To speed up the solution of the problem, the eigenvalues and eigenvectors are computed using the snapshot approach introduced by Sirovich (1987) instead of using the larger-dimensioned direct method (see also Weiss, 2019). Only the 200 most dominant modes are retained for further analysis.

Initial POD analysis applied to the flow field covering up to 3 jets was found to be inadequate in resolving the dynamics of the impinging jets which is primarily due to the uncorrelated motion if the individual jets. An overview on both POD and SPOD applied to the multi-jet measurement domain is provided in the appendix (see Appendix A.2). Thus, to enhance the decomposition, the POD was restricted to a streamwise domain length $x = 5\,D$, roughly bounded by the stagnation points upstream of the rollers formed by each of the impinging jets, e.g. at $x/D \approx -1$ for jet No. 7 with installed arc-conic.

Fig. 10 shows the energy distribution for the first (strongest) 200 modes which barely cover 80% of the energy contained in the flow. The remaining 20% are contained in continuously decreasing smaller scales. The rate of decay follows a -11/9 power law, as indicated by the dashed gray line, and can be attributed to the fully turbulent, nearly iso-tropic flow, especially in the the wall-parallel plane where scales are nearly uniform across the FOV. As shown by Knight & Sirovich (1990) this decay rate in the modal energy spectrum is directly related to classical K41 -5/3 power law of the spatial energy spectrum as introduced by Kolmogorov. For the center plane ($y = 0$) the lower modes depart from this behavior reflecting the spatial variation of scales along with anisotropy of the jet with its shear layers.

Turning to the most energetic spatial modes in Fig. 11 points to differences between the two flow configurations. The strongest mode of the reference case (Fig. 11, a) is a pulsation of the jet fixed to the centerline, followed by a spanwise modulation and roller-like spanwise structures for weaker modes 3 and 4. While the reference case exhibits symmetry of all four modes along the centerplane ($y = 0$), most of the modes of the arc-conics configuration show a varying amount of spanwise asymmetry. Here it should be observed that the mean flow is spanwise symmetric (see Fig. 7, b). Rather, the asymmetry is grounded in a continuous sweeping motion of the jet as highlighted in the velocity time records of Fig. 4(b), where mode 1 is mainly pulsating while mode 2 is more of a

spanwise sweep mode. However, the respective spectral contribution of the reconstructed modes is not provided through this analysis.

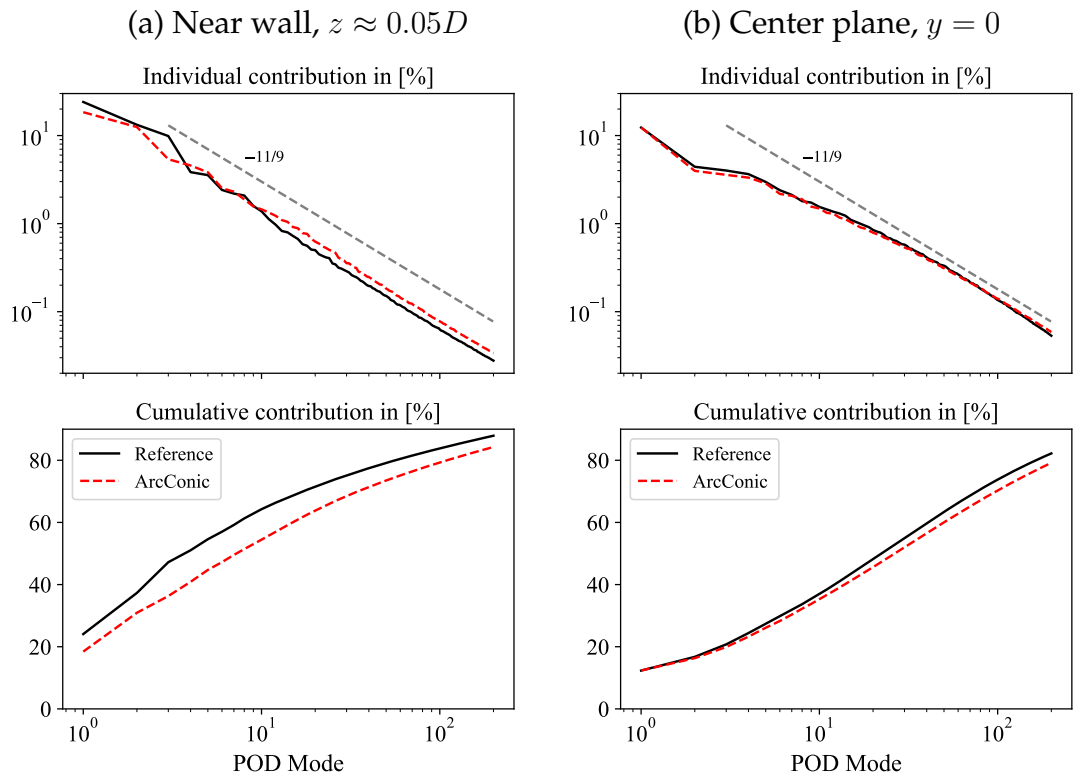

Figure 10. Relative modal energy distribution for the first 200 POD modes on the target plane near jet No. 8 in the wall-parallel plane (a) and center plane (b). The dashed line with slope $-11/9$ is a power law for isotropic turbulence proposed by Knight & Sirovich (1990).

4.5. Modal Analysis using SPOD

The previously described snapshot-based POD provides no information on the spectral content of the flow. As such, the pulsating and sweeping spatial POD modes observed for the impinging jet in Fig. 10 have no frequencies associated with them. Here, spectral proper orthogonal decomposition (SPOD) holds the potential of decomposing the flow field into spatial modes according to their spectral content (Schmidt & Colonius, 2020).

SPOD was performed on the velocity time-records using the *spod_python* package (Burrows, 2020), derived from the Matlab implementation by Schmidt (2022). Similar to the POD, the analysis was focused on the impingement domain of jet No. 8, again on the basis that an analysis covering the entire span of 3 jet intervals "smears" the results (see Appendix A2).

The eigenspectra, that is, the relative spectral contribution of the extracted modes, is plotted in Fig. 12. The solid blue line represents the mean energy spectrum obtained by averaging spectra

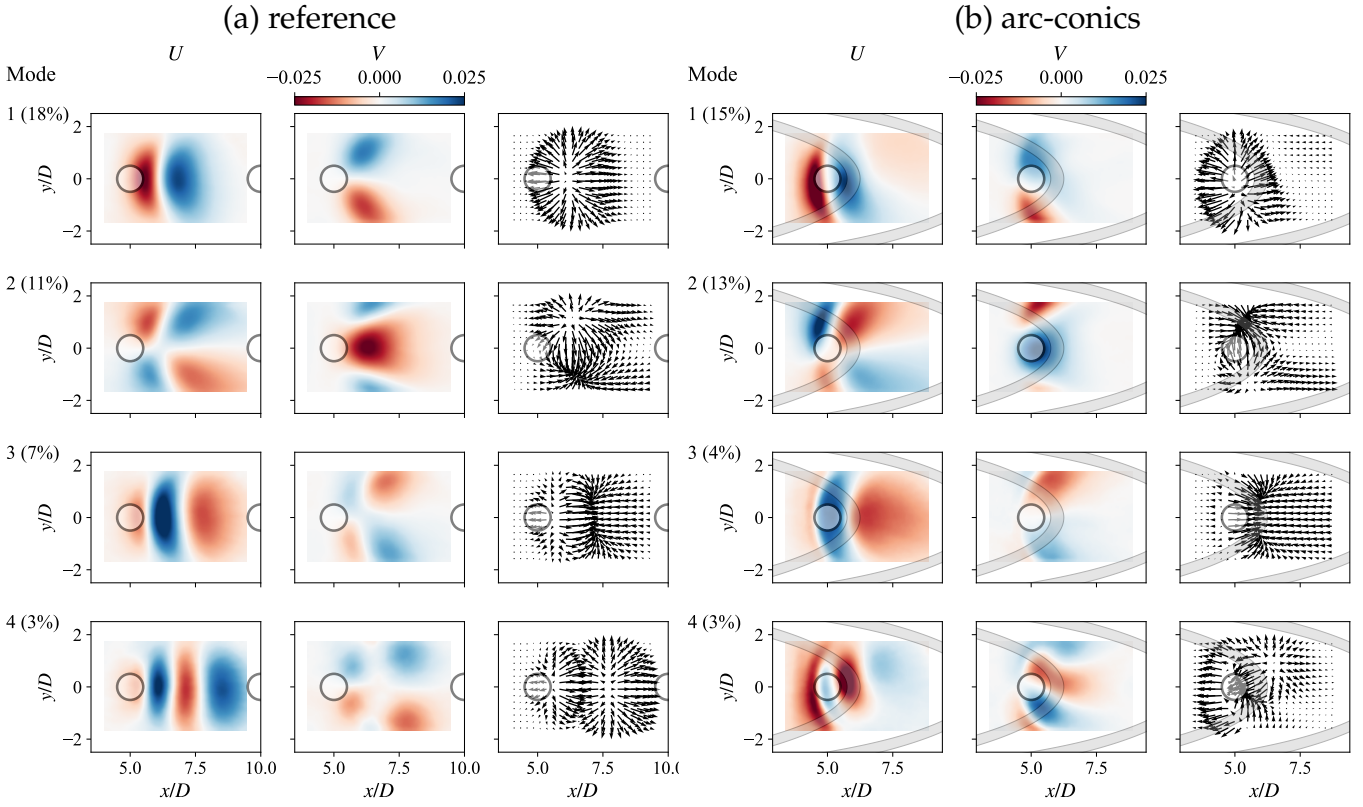

Figure 11. First four POD modes of both configurations obtained in wall-parallel plane ($z \approx 0$) near jet No. 8 for the reference configuration (a) and with arc-conics (b). The relative modal energy contributions are given in [%].

across the domain of $N_x \times N_y = 75 \times 191$ grid points (Welch's method, $N_{FFT} = 2048$, 50% overlap). Whereas the reference case exhibits a classical -5/3 energy cascade, the presence of the arc-conic introduces a low frequency content at $\approx 20\,\mathrm{Hz}$ and a broad-band signal around $200\,\mathrm{Hz}$ to $300\,\mathrm{Hz}$. The roll-up at about $2.5\,\mathrm{kHz}$ is related to the frequency band limit of the PIV processing scheme. Irrespective of the flow condition, the energy-gaps between the modes is nearly featureless, with modes 1 and 2 accounting for more than half the energy. Local maxima in the spectra are selected for the modal reconstructions plotted in Fig. 13. For the reference case, the low frequency modulation at $\approx 18\,\mathrm{Hz}$ is mainly a pulsation of the jet while the arc-conic leads to a pre-dominantly spanwise modulation – also for the higher modes 2 and 3. On the other hand, the spatial modes for the reference case have a high amount of symmetry across the mid-span ($y = 0$). At the higher frequencies (e.g. $266\,\mathrm{Hz}$) the modal structures become more random for the reference case whereas the arc-conic case seems to preserve the signature of the jet's annular shear layer on the surface. In the space-time velocity records of Fig. 4(b) the impingement of these vortex rings can be seen as tightly spaced modulations with opposite angles across the centerline. While spread across a band of frequencies, the continuous, repetitive nature of this interaction is considered one of the main mechanisms of improved heat transfer in the presence of the arc-conic.

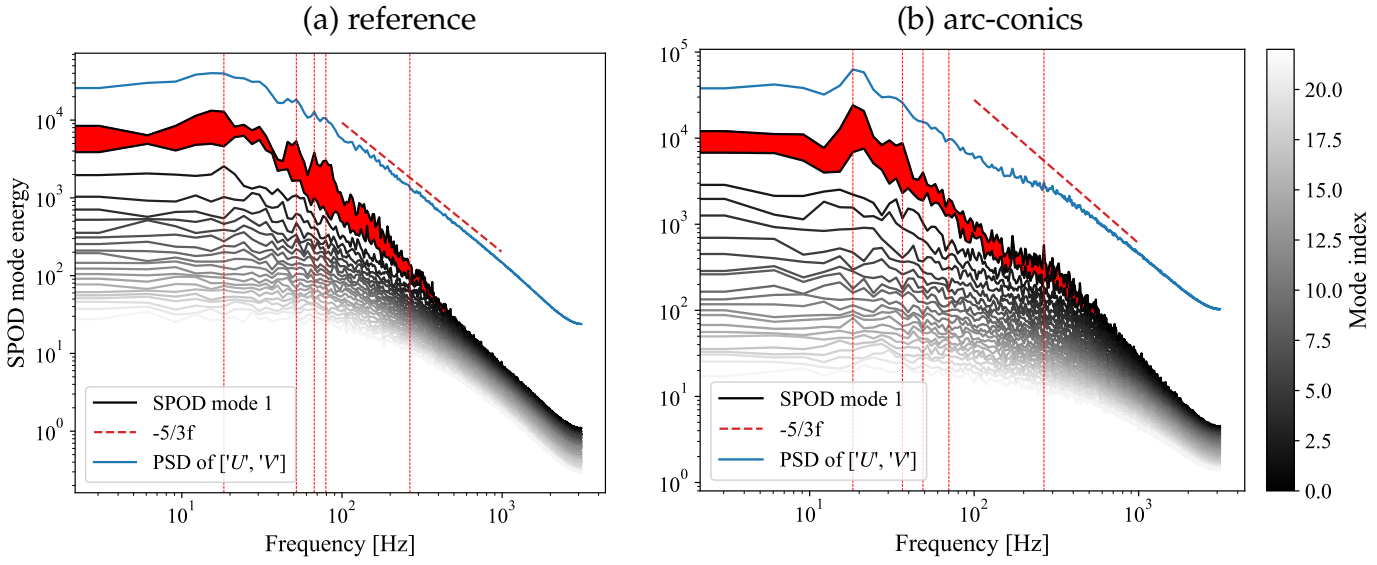

Figure 12. SPOD frequency spectra on the target plane near jet No. 8 for the reference configuration (a), with installed arc-conics (b).

5. Discussion

The results presented in this study highlight several key findings which have implications for the improvement of impingement cooling in combustion-driven turbomachinery. The primary objective was to provide experimental data to validate the numerical simulation (RANS) of a flow configuration with and without structural elements that alter the flow topology and associated

heat transfer. Since the optimization of the structural elements relied on RANS (Brakmann et al., 2023), the unsteady nature of the flow was not accessible, but instead approximated using the given turbulence model. In this regard, 2d-2c HS-PIV provides additional insights to the unsteady flow field allowing the mechanisms of the numerically predicted improved heat transfer to be both visualized and quantified.

The presence of the arc-conics stabilizes the jets, allowing them to continuously deliver fresh cooling air to the surface, even further downstream where the increased streamwise bulk flow causes greater jet deflection in the reference case. High-frequency streaks in the space-time velocity diagrams (Fig. 4, b) suggest a continuous convection of heated fluid away from the jet stagnation point, resulting in a more uniform heat transfer signature across the array of jets.

Part of this investigation focused on the possibilities of reduced order modeling based on modal decomposition to capture the relevant dynamics of the complex impingement flow. Both POD and SPOD were initially found to provide only marginally conclusive information when applied across a large FOV covering a multitude of jets. This is caused by the jet-specific dynamics with practically no inter-jet coupling as already observed in the two-point correlations (see Fig. 9). As a consequence the modal decomposition was performed on individual jet domains, roughly bordered by the mean separation lines on the impingement surface. Even with the reduced analysis domain, the modal decomposition resulted in a large range of modes in both space and time (frequency) reflecting the completely turbulent and stochastic nature of the jet impingement flow. Rather than exhibiting distinct spectral peaks, the frequency spectra feature an energy cascade of the inertial (velocity) scales representative of essentially isotropic turbulence. The presence of the arc-conics is associated with additional low-frequency jet modulation in a pulsating span-wise mode while the pulsation is essentially spanwise-symmetric for the reference case. The previously mentioned high-frequency streaks of Fig. 4(b) are present in the frequency spectra as a wide spectral bump around $200\,\mathrm{Hz}$ to $300\,\mathrm{Hz}$.

Because of the wide range of spatial modes, a reduced order modeling of the flow is believed to be unsuitable to reliably capture the dynamics. It may also explain the surprisingly good performance of simple turbulence models in the numerical simulation of the complex but fully turbulent jet impingement flow.

6. Conclusion & Outlook

The herein presented study focused on the potential of flow altering elements within an inpingement cooling channel configuration. In particular, an arc-conic was added downstream of each jet nozzle with its geometry previously optimized through RANS. High-speed 2d-2c PIV was used to compile an extensive data base for both the arc-conic configuration and a reference case without any modification to the channel geometry. The acquired data set augments previously performed

measurements on the same configuration (Schroll et al., 2022) and features both larger FOVs and longer temporal records, made possible through recent advances in PIV instrumentation, in particular concerning HS-cameras and lasers. The acquired velocity data sets are well suited to provide converged velocity statistics and enable spatial correlations as well as modal decomposition, both spatial and temporal.

Concerning the flow topology, the arc-conics capture the cross-flow redirecting it toward the target plate while at the same time stabilizing the jets, especially toward the channel exit where the jets exhibit an increasing tendency toward lift-off in the unmodified reference configuration. In effect, the arc-conics lead to a more uniform jet impingement pattern across the jets, confirming the predictions by RANS. Two-point correlation on the velocity data revealed essentially no interaction between neighboring jets or beyond, suggesting that each jet acts on its own with its own dynamics. This may be due to the spanwise confinement of the jets and configurations featuring 2d jet arrays may behave completely different, while the arc-conics will most likely dampen the otherwise unconfined jet dynamics.

The jet-specific dynamics required the application of modal decomposition to be restricted to the domains of single jet intervals. In spite of this, reduced order modelling of impingement flow on basis of POD and SPOD had limited success with the energy content spread across a large number of modes and is grounded in the fully turbulent, highly stochastic nature of the jet-impingement flow. This has implications on numerical models and also explains reasonable performance of conventional RANS modelling in this context. Among the dominant modes recovered with POD and SPOD are pulsating modes and spanwise sweeping motions, both of which become more regular in the presence of the arc-conics. Additional energy content at higher frequencies of the arc-conic configuration is attributed to the jet's shear layer directly interacting with the target plate, continuously introducing cool air and is considered one of the primary mechanisms for the improved heat transfer.

Unfortunately measurements of the spatial temperature distribution are not available, so the numerically predicted Nusselt number distribution could not be determined experimentally. Here, the utilization of unsteady temperature sensitive paint (iTSP), as reported by Schroll et al. (2022), could provide this information and is being actively considered. An alternative approach could be to estimate heat transfer (or temperature distribution) from the unsteady near-wall flow data, as also previously reported by Schroll et al. (2022). This correlation-based approach could be validated on the basis of existing LES of the same configuration (Morsbach et al., 2024) and then applied to the arc-conic configuration for which an additional LES would become prohibitively expensive, in particular when performing simulations on the even more complex cooling configurations of actual turbomachinery components.

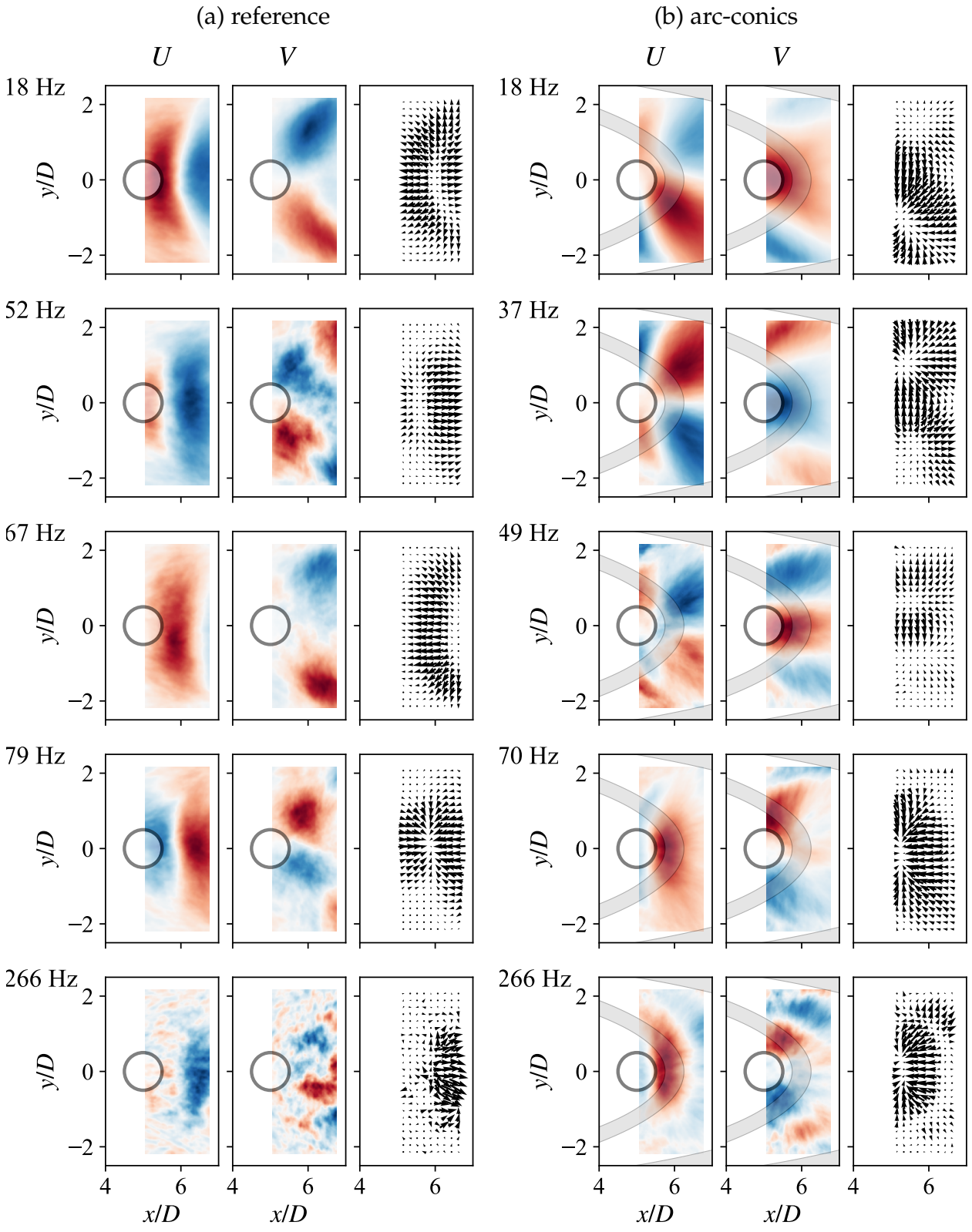

Figure 13. SPOD modes for selected frequencies in wall-parallel plane ($z \approx 0$) near jet No. 8 for the reference configuration (a) and with arc-conics (b). See Fig. 12 for corresponding spectra.

Appendix

A.1 POD on multiple jets

As mentioned in Sec. 4.4 a sampling domain simultaneously capturing a multitude of jets leads to a reduced contribution of each proper orthogonal decomposition (POD) mode with the first mode barely exceeding $5\,\%$ (see Fig. 14). This is also reflected in mode distributions presented in Fig. 15 where self-similar features appear at different jets for different modes at similar energetic levels. As a consequence the modal analysis was restricted to an area of a single jet interval.

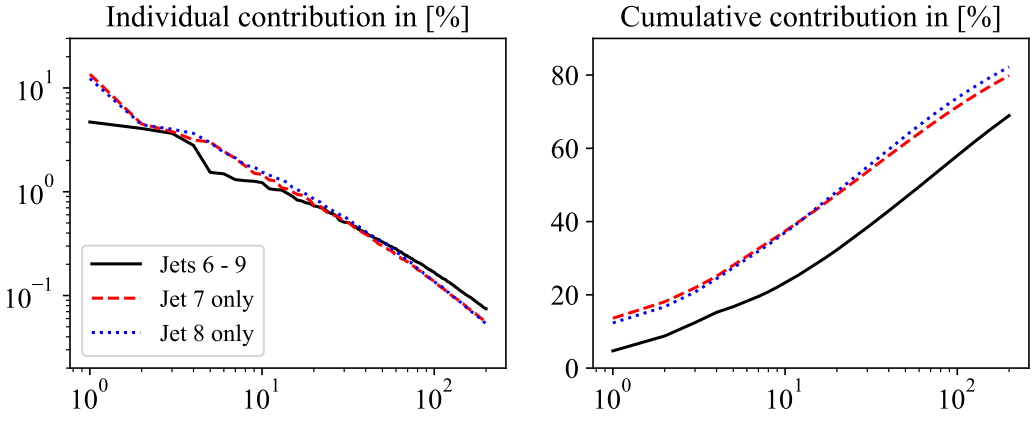

Figure 14. POD modal energies in the symmetry plane ($y = 0$) obtained for the reference case covering jets No. 6 to No. 9 (solid line) compared to POD applied to single jets.

A.2 SPOD on multiple jets

Similar to the POD analysis, the spectral proper orthogonal decomposition (SPOD) on the full domain of three jets attenuates dynamics that are uncovered by restricting the analysis to a single jet only. Unlike Fig. 12, the mode energy spectra in Fig. 16 show no specific signatures across the frequency domain; the gap between first and second mode is not particularly pronounced. This is also reflected in the reconstructed modes of Fig. 17, with similar patterns appearing for different frequencies at different jets, indicating different dominant frequencies from jet to jet.

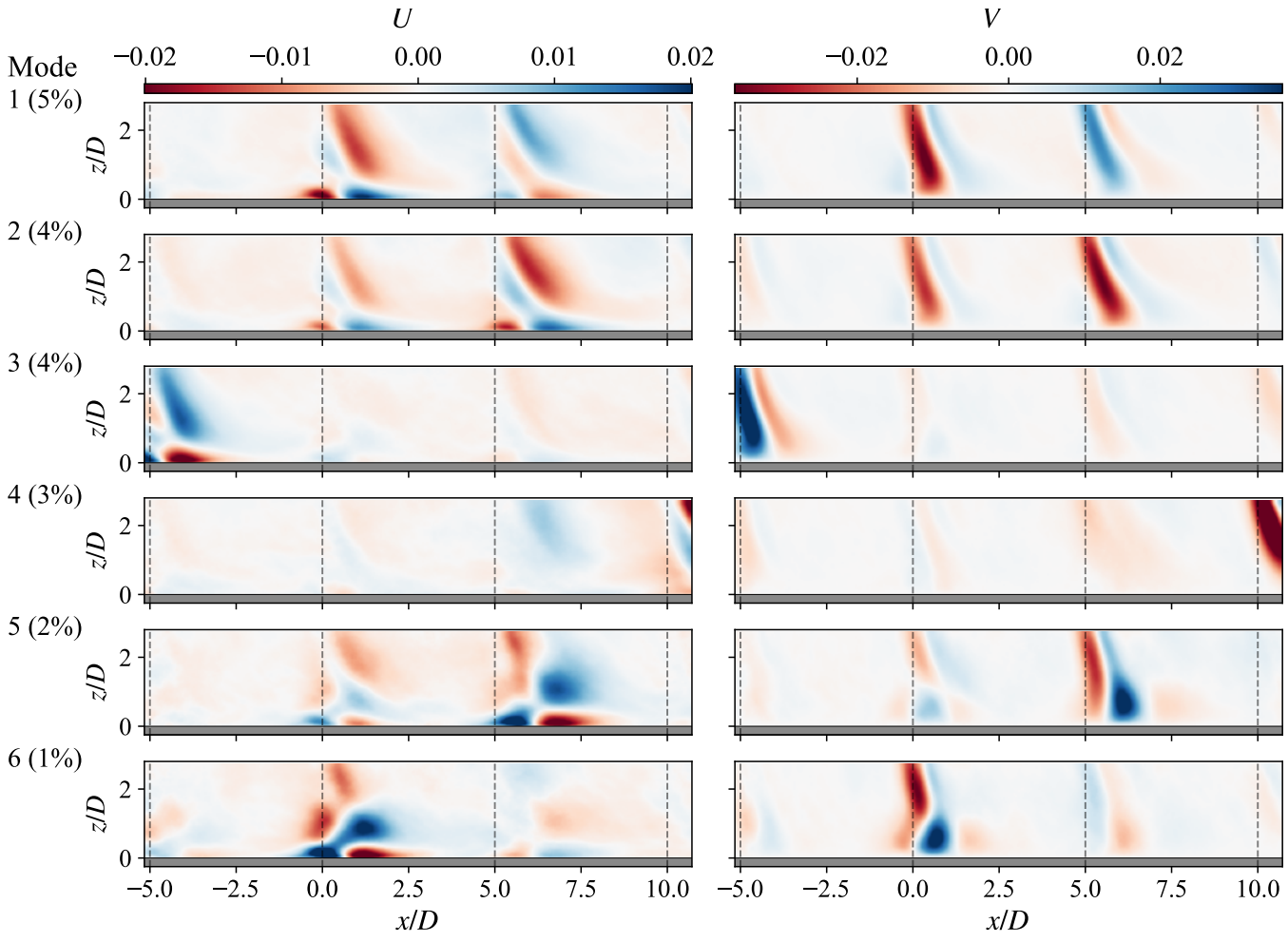

Figure 15. First 6 POD modes in the symmetry plane ($y = 0$) obtained for the reference case using a FOV covering jets No. 6 to No. 9.

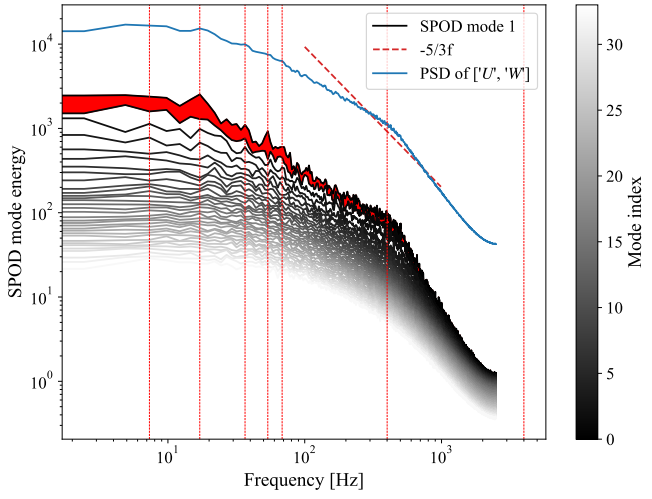

Figure 16. SPOD energy spectra obtained for the reference case using a FOV covering jets No. 6 to No. 9.

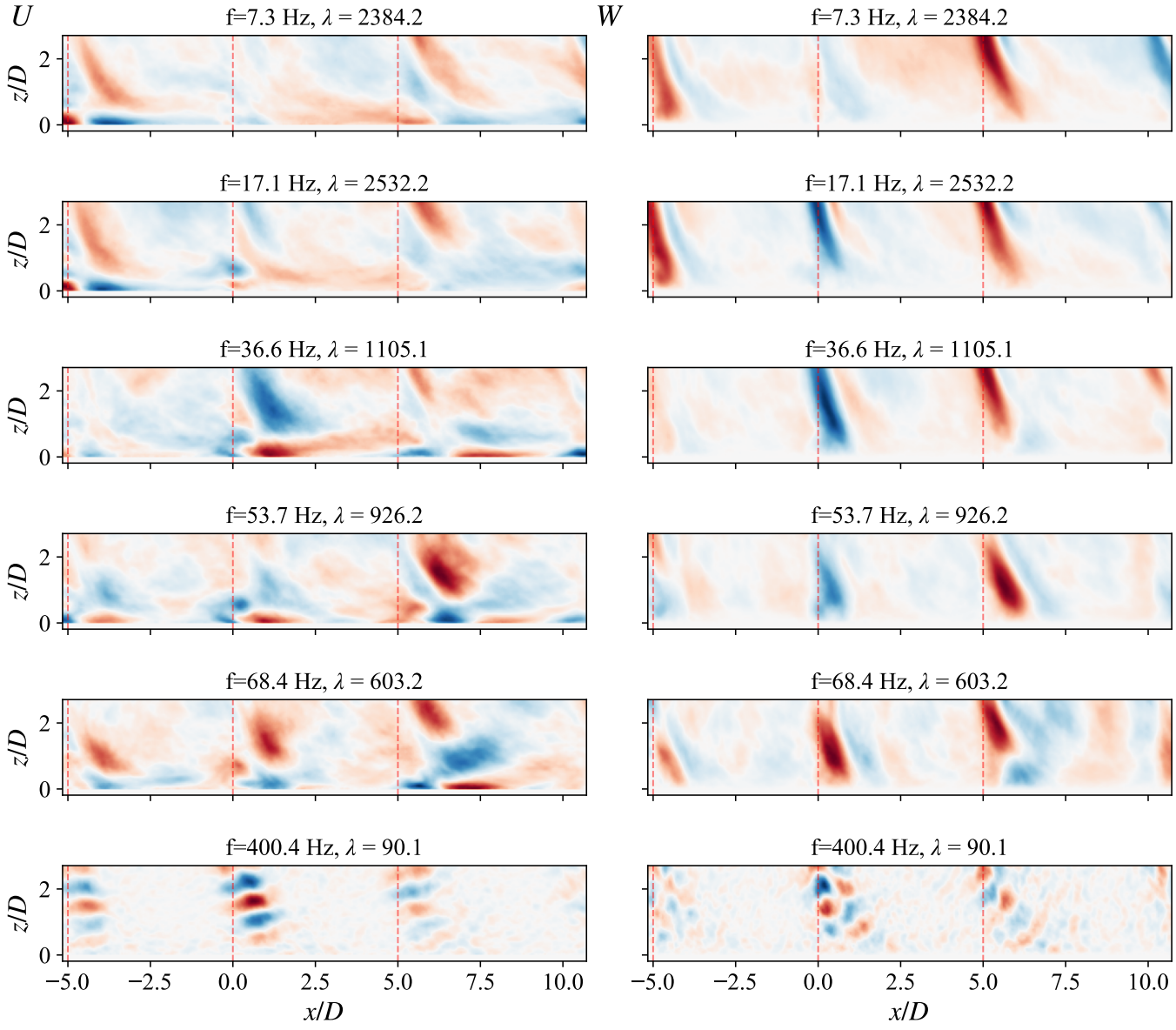

Figure 17. Selected modes of the SPOD obtained in the symmetry plane ($y = 0$) for the reference case in using a FOV covering jets No. 6 to No. 9 for frequencies shown in Fig. 16.

References

Brakmann, R. G., Brose, N., Carvalho, F., Chargui, S., & Guarino, R. (2023, 06). A numerical analysis of cross-flow reinforced impingement cooling with a u-shaped flow-guide on the hole plate. In *Turbo Expo: Power for Land, Sea, and Air* (Vol. Volume 7B: Heat Transfer - General Interest/Additive Manufacturing Impacts on Heat Transfer; Internal Air Systems; Internal Cooling, p. V07BT15A003). doi: 10.1115/GT2023-101097

Burrows, T. J. (2020). *Python spod code.* `https://github.com/tjburrows/spod_python`. GitHub. Retrieved from `https://github.com/tjburrows/spod_python`

Depardon, S., Lasserre, J., Boueilh, J., Brizzi, L., & Borée, J. (2005). Skin friction pattern analysis using near-wall PIV. *Experiments in Fluids*, *39*(5), 805 – 818. doi: 10.1007/s00348-005-0014-8

Knight, B., & Sirovich, L. (1990). Kolmogorov inertial range for inhomogeneous turbulent flows. *Physical Review Letters*, *65*(11), 1356–1359. Retrieved 2023-05-12, from `https://link.aps.org/doi/10.1103/PhysRevLett.65.1356` doi: 10.1103/PhysRevLett.65.1356

Morsbach, C., Matha, M., Brakmann, R., Tabassum, S., Bergmann, M., Schroll, M., … E., K. (2024). Investigating the unsteady dynamics of a multi-jet impingement cooling flow using large eddy simulation. In *ASME Turbo Expo 2024: Turbomachinery Technical Conference and Exposition.* London, United Kingdom.

Pedregosa, F., Varoquaux, G., Gramfort, A., Michel, V., Thirion, B., Grisel, O., … Duchesnay, E. (2011). Scikit-learn: Machine learning in Python. *Journal of Machine Learning Research*, *12*, 2825–2830. Retrieved from `https://www.jmlr.org/papers/v12/pedregosa11a.html`

Perry, A. E., & Chong, M. S. (1987). A description of eddying motions and flow patterns using critical-point concepts. *Ann. Rev. Fluid Mech.*, *19*, 125-155.

Schmidt, O. T. (2022). *Spectral proper orthogonal decomposition in matlab.* `https://github.com/SpectralPOD/spod_matlab`. GitHub. Retrieved from `https://github.com/SpectralPOD/spod_matlab`

Schmidt, O. T., & Colonius, T. (2020). Guide to spectral proper orthogonal decomposition. *AIAA Journal*, *58*(3), 1023–1033. Retrieved 2021-05-19, from `https://arc.aiaa.org/doi/10.2514/1.J058809` doi: 10.2514/1.J058809

Schroll, M., Klinner, J., Müller, M., Matha, M., Hilfer, M., Tabassum, S., … Willert, C. (2022, Juli). Experimental and numerical investigation of a multi-jet impingement cooling configuration. In *20th International Symposium on Application of Laser and Imaging Techniques to Fluid Mechanics.* Retrieved from `https://elib.dlr.de/187567/`

Shavit, U., Lowe, R., & Steinbuck, J. (2007). Intensity capping: a simple method to improve cross-correlation piv results. *Experiment in Fluids*, *42*, 225–240. Retrieved from https://doi.org/10.1007/s00348-006-0233-7 doi: 10.1007/s00348-006-0233-7

Sirovich, L. (1987). Turbulence and the dynamics of coherent structures part iii: dynamics and scaling. *Quarterly of Applied Mathematics*, *45*(3), 583–590. Retrieved 2023-05-09, from http://www.jstor.org/stable/43637459 doi: 10.2307/43637459

Tabassum, S., Hilfer, M., Brakmann, R. G., Morsbach, C., Willert, C., Matha, M., & Schroll, M. (2023). Assessment of Computational Fluid Dynamic Modeling of Multi-Jet Impingement Cooling and Validation With the Experiments. *Journal of Turbomachinery*, *145*(7), 071005. doi: 10.1115/1.4056715

Weiss, J. (2019). A tutorial on the proper orthogonal decomposition. In *AIAA Aviation 2019 Forum*. Dallas, Texas: American Institute of Aeronautics and Astronautics. Retrieved 2023-04-17, from https://arc.aiaa.org/doi/10.2514/6.2019-3333 doi: 10.2514/6.2019-3333

Westerweel, J., & Scarano, F. (2005). Universal outlier detection for PIV data. *Experiments in Fluids*, *39*(6), 1096-1100. Retrieved from http://dx.doi.org/10.1007/s00348-005-0016-6 doi: 10.1007/s00348-005-0016-6